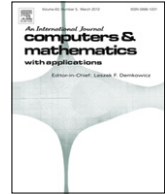




Contents lists available at ScienceDirect

Computers and Mathematics with Applications

journal homepage: www.elsevier.com/locate/camwa

Benchmarking the Dirac-generated unitary lattice qubit collision-stream algorithm for 1D vector Manakov soliton collisions

Armen Oganessov^a, George Vahala^{a,*}, Linda Vahala^b, Jeffrey Yepez^{c,d},
Min Soe^e

^a Department of Physics, William & Mary, Williamsburg, VA 23185, United States

^b Department of Electrical & Computer Engineering, Old Dominion University, Norfolk, VA 23529, United States

^c Air Force Research Laboratory/Directed Energy, Air Force Maui Optical & Supercomputing Observatory, Kihei, HI 96753, United States

^d Department of Physics and Astronomy, University of Hawai'i at Manoa Watanabe Hall, 2505 Correa Road, Honolulu, HI 96822, United States

^e Department of Mathematics and Physical Sciences, Rogers State University, Claremore, OK 74017, United States

ARTICLE INFO

Article history:

Available online xxxx

Keywords:

Unitary quantum lattice gas

Qubits

1D Manakov solitons

ABSTRACT

The unitary quantum lattice gas (QLG) algorithm is a mesoscopic unitary perturbative representation that can model the mean field Gross Pitaevskii equation for the evolution of the ground state wave function of Bose Einstein Condensates (BECs). The QLG considered here consists of an interleaved sequence of unitary collide-stream operators, with the collision operator being deduced from that for the Dirac equation, with the nonlinear potentials of the BECs being the mass term in the Dirac equation. Since the unitary collision operator is more accurate one obtains a more accurate representation of the nonlinear terms. Further benchmark QLG simulations are reported here: that for the exactly soluble 1D vector Manakov soliton collisions. It is found that this Dirac-based unitary algorithm permits simulations with vector soliton parameters (soliton amplitudes and speeds) that are considerably greater than those achieved under our previous $\sqrt{\text{SWAP}}$ QLG algorithm.

© 2015 Elsevier Ltd. All rights reserved.

1. Introduction

Quantum entanglement is the vine from which branches the field of quantum computing and quantum information theory whose building blocks are qubits. Unlike the classical binary bit, which can only take on the value of “0” or “1”, the qubit state exists as a superposition of these classical states “0” and “1”. In particular, the qubit $|q\rangle$

$$|q\rangle = \gamma_0|0\rangle + \gamma_1|1\rangle \quad \text{with } |\gamma_0|^2 + |\gamma_1|^2 = 1 \quad (1)$$

where γ_0 , and γ_1 are complex probability amplitudes. For quantum entanglement, the minimum structure on which we operate is the two qubits, with representation

$$|q_1q_2\rangle = \gamma_{00}|00\rangle + \gamma_{01}|01\rangle + \gamma_{10}|10\rangle + \gamma_{11}|11\rangle. \quad (2)$$

* Corresponding author.

E-mail address: gvahala@gmail.com (G. Vahala).

<http://dx.doi.org/10.1016/j.camwa.2015.06.001>

0898-1221/© 2015 Elsevier Ltd. All rights reserved.

While the more traditional approach to quantum dynamics is through Hamiltonians or Lagrangians, a novel approach – first introduced by Feynman [1,2] – is through qubit dynamics. A very immediate advantage of these qubit representations is that they permit close to ideal parallelization on even classical supercomputers.

The quantum lattice gas (QLG) is one of the earliest unitary algorithms [3–13] that under appropriately interlaced sequence of unitary entangling collision operators and unitary streaming operators can, in the long wavelength limit, recover the physics under investigation [14]. Here, we further benchmark our Dirac-based QLG algorithm [15] for the 1D vector Manakov soliton collisions [16–20]. A somewhat related alternate approach has been considered by Succi and his collaborators [21–25]. In the Succi approach, the Majorana representation of the Dirac matrices is considered—and these matrices are real, while in the Yepez approach one uses the complex chiral representation. The Succi approach has a formal analog with the quantum lattice Boltzmann (which is non-unitary) while in the Yepez-formulation there is a connection made with qubits and quantum information (which is unitary).

Mode propagation in optical fibers can play a dominant role in long-distance communication. Optical fibers are typically birefringent, with a single-mode fiber permitting two orthogonal polarizations: the so-called O-mode which has a constant refractive index along its ray path, while the X-mode has a refractive index that varies along its ray path. It has been shown [16] that the slowly varying amplitudes of these modes can be determined from the 1D coupled-NLS equations

$$i\partial_t Q_1 = -\partial_{xx} Q_1 - 2\mu[|Q_1|^2 + B|Q_2|^2]Q_1, \quad i\partial_t Q_2 = -\partial_{xx} Q_2 - 2\mu[|Q_2|^2 + B|Q_1|^2]Q_2, \tag{3}$$

where $\mu > 0$, and B is the cross-phase birefringence modulation coefficient, $2 \leq 3B \leq 6$. It has been shown for the special case of $B = 1$, that this coupled-NLS equation (3) is completely integrable [16–18] and is known as the Manakov equations. In particular, exact 2-soliton vector solutions of the Manakov equations (3) are [16]

$$\begin{pmatrix} Q_1(x, t) = \sum_{n=1}^2 \frac{1}{2} \alpha_n \exp\left(-\frac{1}{2} + i\eta_{nl}\right) \operatorname{sech}\left[\eta_{nR} + \frac{1}{2}R_n\right] \\ Q_2(x, t) = \sum_{n=1}^2 \frac{1}{2} \beta_n \exp\left(-\frac{1}{2} + i\eta_{nl}\right) \operatorname{sech}\left[\eta_{nR} + \frac{1}{2}R_n\right] \end{pmatrix}, \tag{4}$$

where α_n, β_n and k_n are arbitrary complex parameters with $(n = 1, 2)$

$$\eta_n = \eta_{nR} + i\eta_{nl} = k_n(x - x_{0n} + ik_n t), \quad R_n = \ln\left[\frac{\mu(|\alpha_n|^2 + |\beta_n|^2)}{4k_{nR}^2}\right]. \tag{5}$$

For each propagating mode, the (real) parameters x_{0n} predominantly determine the location of the soliton peaks if the two solitons are non-overlapping, while k_{nR} predominantly dictate the individual soliton amplitudes and k_{nl} the soliton speeds.

The asymptotic post-collision vector soliton solutions have been determined [16–18] for times when there are no non-overlapping solitons. In particular for $k_{nR} > 0$, the post-collision non-overlapping 2-soliton amplitudes are given by (where ‘ denotes post-collision state properties)

$$\begin{pmatrix} \frac{\alpha'_1}{\beta'_1} = \left(\left[1 - g + \left| \frac{\alpha_1}{\beta_1} \right|^2 \right] \frac{\alpha_2}{\beta_2} \right) \left(g \frac{\alpha_1^*}{\beta_1^*} \frac{\alpha_2}{\beta_2} + (1 - g) \left| \frac{\alpha_1}{\beta_1} \right|^2 + 1 \right)^{-1} \\ \frac{\alpha'_2}{\beta'_2} = \left(\left[1 - h + \left| \frac{\alpha_2}{\beta_2} \right|^2 \right] \frac{\alpha_1}{\beta_1} \right) \left(h^* \frac{\alpha_2^*}{\beta_2^*} \frac{\alpha_1}{\beta_1} + (1 - h^*) \left| \frac{\alpha_2}{\beta_2} \right|^2 + 1 \right)^{-1} \end{pmatrix} \tag{6}$$

where

$$g(k_1, k_2) = \frac{2k_{1R}}{k_2 + k_1^*}, \quad h(k_1, k_2) = \frac{2k_{2R}}{k_1 + k_2^*}. \tag{7}$$

Radhakrishnan et al. [16] showed analytically that for certain parameter choices there exists inelastic vector soliton solutions—i.e., in a vector collision of 2-soliton polarization states, one of the soliton pairs in a particular polarization is annihilated. This type of inelastic collision is impossible in scalar NLS theory because of the normalization constraints

$$\int |Q_i(x, t)|^2 dx = \text{const}, \quad i = 1, 2. \tag{8}$$

Moreover the k_n are collisional invariants. Thus, for a particular choice of parameters the post-collision amplitudes for the Q_1 -polarization will have (see also Fig. 1)

$$\alpha'_1 = 0, \quad \text{but} \quad \alpha'_2 \neq 0. \tag{9}$$

It is just this type of inelastic collision that led to the idea of using inelastic Manakov solitons for digital information processing in a nonlinear optical medium without radiation losses [17–19].

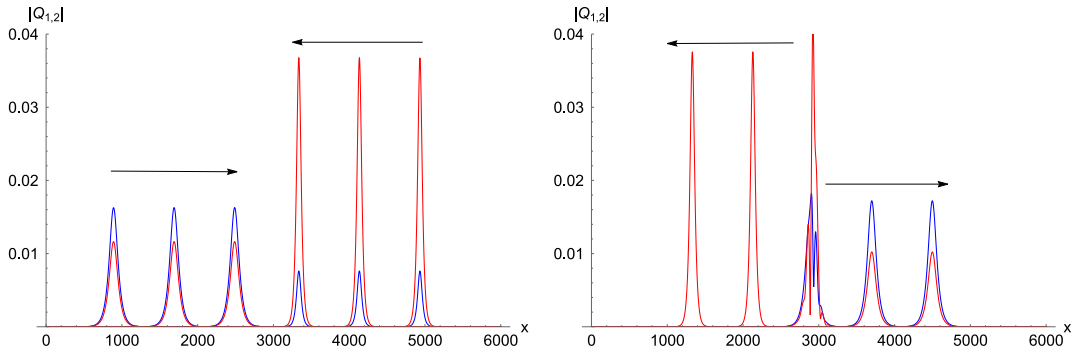


Fig. 1. The collisional evolution of Manakov solitons of relatively small amplitudes and speeds. *left figure* The pre-collision states at $t = 0$, $t = 10K$, $t = 20K$ while the post-collision states *right figure* are at times $t = 25K$, $t = 35K$, $t = 45K$. The first polarization amplitude 2-soliton $|Q_1(x, t)|$ is in blue, while the orthogonal polarization 2-soliton $|Q_2(x, t)|$ is in red. The inelastic soliton collision occurs for specially chosen soliton amplitudes and speeds, and in this case the post-collision soliton for $|Q_1(x, t)| = 0$ for $x < 3000$ is totally absent. Simulations performed on a grid $L = 6000$ is totally absent. Simulations performed on a grid $L = 6000$ is totally absent, under periodic boundary conditions. (For interpretation of the references to color in this figure legend, the reader is referred to the web version of this article.)

The QLG algorithm is a perturbative unitary algorithm. Depending on the choice and sequence of (non-commuting) collide-stream operators on the qubit states, one can recover in the long wavelength limit various equations of physics, not unlike its distant cousin the lattice Boltzmann algorithm that has been used to model the Navier–Stokes equations, Burgers equation, magnetohydrodynamics, colloidal flows, micro fluid flows to list the most important [26]. Here we concentrate on two QLG algorithms that will recover the coupled NLS equations (3). The first algorithm utilized the $\sqrt{\text{SWAP}}$ gate and required the introduction of the nonlinear terms in (3) as a separate distinct rotation [20]. While successful, the perturbative aspects of the algorithm did not permit extension of this representation to considerably higher amplitude solitons. This could be attributable to the fact that the unitary $\sqrt{\text{SWAP}}$ collide-stream unitary sequence just generated the ∇^2 in the long wavelength limit, and the unitary phase rotation introduced the nonlinearities. Here we will utilize the unitary QLG algorithm developed by Yezep [27,28] for the relativistic Dirac particle in 3D by incorporating a Lorentz mass scalar as an effective potential. This new unitary collision operator will replace both the $\sqrt{\text{SWAP}}$ and the phase rotation in the older QLG algorithm [20]. We shall see that this will permit successful simulations of the Manakov solitons at significantly higher amplitudes than were previously permitted. This opens up the possibilities of utilizing this new QLG to study complex quantum vortex structures in 3D spinor BECs.

2. QLG algorithm using the unitary $\sqrt{\text{SWAP}}$ collision operator

QLG is a unitary mesoscopic lattice algorithm with interleaved collision-stream operators: the unitary collision operator locally entangles the qubit amplitudes while the unitary stream operator transports that entanglement throughout the spatial lattice. One introduces two qubits per scalar field and need only work in the 1-body subspace $|01\rangle, |10\rangle$ of each scalar field. The local $\sqrt{\text{SWAP}}$ collision operator in this subspace has the form

$$C = \exp \left[i \frac{\pi}{4} \sigma_x (1 - \sigma_x) \right] = \frac{1}{2} \begin{pmatrix} 1 - i & 1 + i \\ 1 + i & 1 - i \end{pmatrix}, \tag{10}$$

where the σ are the Pauli spin matrices

$$\sigma_x = \begin{pmatrix} 0 & 1 \\ 1 & 0 \end{pmatrix}, \quad \sigma_y = \begin{pmatrix} 0 & -i \\ i & 0 \end{pmatrix}, \quad \sigma_z = \begin{pmatrix} 1 & 0 \\ 0 & -1 \end{pmatrix}. \tag{11}$$

The corresponding scalar wave function (dropping the subscript label for simplicity) at lattice site \mathbf{x}

$$\Phi(\mathbf{x}, t) = \begin{pmatrix} \gamma_{01}(\mathbf{x}, t) \\ \gamma_{10}(\mathbf{x}, t) \end{pmatrix}. \tag{12}$$

The local qubit entanglement at \mathbf{x} is propagated throughout the lattice by the unitary streaming operators

$$S_{\Delta\mathbf{x},0} = n + e^{\Delta\mathbf{x}\partial_{\mathbf{x}}} \bar{n}, \quad S_{\Delta\mathbf{x},1} = \bar{n} + e^{\Delta\mathbf{x}\partial_{\mathbf{x}}} n, \tag{13}$$

$n = \frac{1}{2}(1 - \sigma_z)$ and $\bar{n} = \frac{1}{2}(1 + \sigma_z)$ with a shift in the components of Φ along the lattice directions $\pm \Delta\mathbf{x}$, respectively. Basically, (13) unitarily shifts just one of these post-collision excited state amplitude probability to the nearest neighbor lattice site $\mathbf{x} \pm \Delta\mathbf{x}$, respectively. In particular, let us first consider the evolution operator for the κ th component of Φ . Consider a QLG algorithm that interleaves the noncommuting collide and stream operators, $[S_{\Delta\mathbf{x},\kappa}, C] \neq 0$,

$$I_{\kappa\kappa} = S_{-\Delta\mathbf{x},\kappa} C S_{\Delta\mathbf{x},\kappa} C \tag{14}$$

where κ is either 0 or 1 corresponding to the streaming of either the γ_{01} or γ_{10} component of Φ in (12). One proceeds similarly with the other scalar field in the coupled NLS equation (3).

In the evolution operator for the κ component of scalar wave function Φ one introduces the nonlinear potential Ω as a phase rotation

$$U_\kappa[\Omega(\mathbf{x})] = I_{x\kappa}^2 \exp[-i\varepsilon^2 \Omega(\mathbf{x})], \tag{15}$$

where Ω will later be chosen as the corresponding nonlinear coupling potential in Eq. (3). ε is a small perturbative parameter. The final quantum map that evolves the components Φ_n of the vector wave function is

$$\Phi_n(\mathbf{x}, t + \Delta t) = U[\Omega_n(\mathbf{x})] \Phi_n(\mathbf{x}, t), \quad \text{with } U[\Omega_n] = U_1 \left[\frac{\Omega_n}{2} \right] U_0 \left[\frac{\Omega_n}{2} \right]. \tag{16}$$

Thus to recover the 1D Manakov vector NLS equation (3) from this mesoscopic quantum map, one must choose parameters such that the quantum map obeys diffusion ordering, with $\Delta \mathbf{x} \sim \varepsilon$, $[\Phi_n(\mathbf{x}, t + \Delta t) - \Phi_n(\mathbf{x}, t)] \rightarrow \varepsilon^2 \partial_t \Phi_n(\mathbf{x}, t)$, and contracts the 2-component field Φ_n to the scalar 1D NLS wave function $Q_n = (1, 1) \cdot \Phi_n = \gamma_{01,n} + \gamma_{10,n}$. The nonlinear potential terms are chosen $\Omega_1 = 2\mu[|Q_1|^2 + B|Q_2|^2]$ and $\Omega_2 = 2\mu[|Q_2|^2 + B|Q_1|^2]$. The extension to 3D is straightforward: all one needs to do is to extend the interleaving operator along each orthogonal lattice direction: $I_{x\kappa}^2 I_{y\kappa}^2 I_{z\kappa}^2$.

3. QLG using the alternate unitary collision operator based on the Dirac equation

Yepez first developed a unitary QLG algorithm for the 3D relativistic Dirac particle dynamics [27] and then extended it by adding an effective potential as a Lorentz mass scalar [28]. To model the Manakov vector NLS equation (3) we simply take the nonrelativistic limit of this unitary Dirac collision operator and identify the mass term with the nonlinear interactions of the Manakov equation (3). This new collision operator $C_{D,n}$, Eq. (17), replaces both the $\sqrt{\text{SWAP}}$ collision operator and the phase rotation used to implement the nonlinear potential in the old QLG algorithm [20]:

$$C_{D,n} = \begin{pmatrix} \cos \theta_n(x) & -i \sin \theta_n(x) \\ -i \sin \theta_n(x) & \cos \theta_n(x) \end{pmatrix}, \tag{17}$$

with

$$\theta_n(x) = \frac{\pi}{4} - \frac{1}{8} \Omega_n^2, \quad n = 1, 2 \tag{18}$$

and the nonlinear interaction terms $\Omega_1 = 2\mu[|Q_1|^2 + B|Q_2|^2]$ and $\Omega_2 = 2\mu[|Q_2|^2 + B|Q_1|^2]$. The inter-leavened sequence of non-commuting unitary collide-stream operators is as in the old QLG algorithm. The nonlinear potential Ω_n is now an integral part of the collision operator itself and is not just an extra exponential phase factor as in (15). The most important consequence of using this nonrelativistic unitary Dirac collision operator $C_{D,n}$ in the QLG algorithm is that our simulations can run up to an order of magnitude greater than can be achieved by the $\sqrt{\text{SWAP}}$ unitary collision operator QLG.

3.1. Manakov solitons simulations—benchmark against $\sqrt{\text{SWAP}}$ QLG algorithm

We first validate our Dirac-based collisional QLG algorithm to show that we can recover our earlier inelastic Manakov results using the same order of magnitude initial soliton speeds and amplitudes as could be obtained in the $\sqrt{\text{SWAP}}$ unitary collision QLG algorithm. In Fig. 1, we show the pre-collision and post-collision 2-soliton pairs ($|Q_1(x, t)|$ in blue, and $|Q_2(x, t)|$ in red), with the arrows giving the propagation directions. At $t = 0$, the vector 2-soliton pairs are centered around $x = 900$ and $x = 5000$. For specially chosen initial parameters, there is an inelastic collision as is seen in the disappearance of the soliton in the post-collision state of $|Q_1(x, t)|$ that is propagating to the left (see the left figure of Fig. 1).

However, after the next soliton collision the amplitudes will no longer satisfy the criterion for an inelastic collision, Eq. (9), and the $|Q_1(x, t)|$ 2-solitons will reappear. In Fig. 2, we plot the time evolution of the 2-soliton maxima (i.e., the $\max_{1 \leq x \leq L} |Q_n(x, t)|$, $n = 1, 2$) throughout the run (here $t_{max} = 400K$). The higher amplitude soliton is shown dashed, to distinguish it from the lower amplitude soliton. The spikes in the peaks occur during soliton-soliton overlap. The inelastic collision, resulting in the loss of the lower amplitude soliton in $|Q_1|$ is clearly seen after the 1st soliton-soliton collision around $t = 25K$, see also Fig. 1, but it reappears after the 2nd soliton-soliton collision. In the time intervals between soliton-soliton collisions the four soliton shape, amplitude and speed remains invariant as can be seen in Figs. 1 and 2. There is no second inelastic vector soliton-soliton collision in $|Q_1|$ around $t = 330K$, although the secondary soliton peak is quite low, around 2×10^{-4} .

The intensity spectrum in each mode is shown for the integrable Manakov vector solitons in Fig. 3.

3.2. Higher amplitude vector Manakov soliton collisions

We now increase the soliton amplitudes to levels that cannot be handled by our older $\sqrt{\text{SWAP}}$ QLG algorithm on this grid. Again, we choose parameters so that there will be a Manakov inelastic first collision among the vector soliton modes, i.e.,

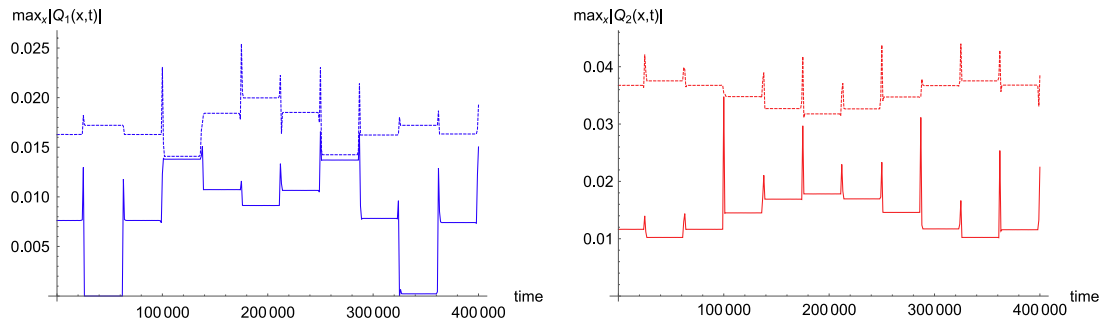


Fig. 2. A plot of the time evolution of the vector 2-soliton peaks, $\max_{1 \leq x \leq L} |Q_n(x, t)|$, $n = 1, 2$, in each mode. Vector soliton–soliton collisions occur whenever the peaks spike. For the parameters chosen, an inelastic Manakov soliton collision occurs only for $t \sim 24K$, with the subsequent loss of one of the solitons. This soliton reappears following the next vector soliton–soliton overlap collision. The dashed curves are for the higher amplitude soliton within that particular mode, while the solid curve is for the lower soliton amplitude. For the integrable Manakov system the vector 2-soliton solution exhibits invariant soliton properties away from the collisional overlap regions: i.e., the constant horizontal sections indicate the non-overlapping soliton spatial regions.

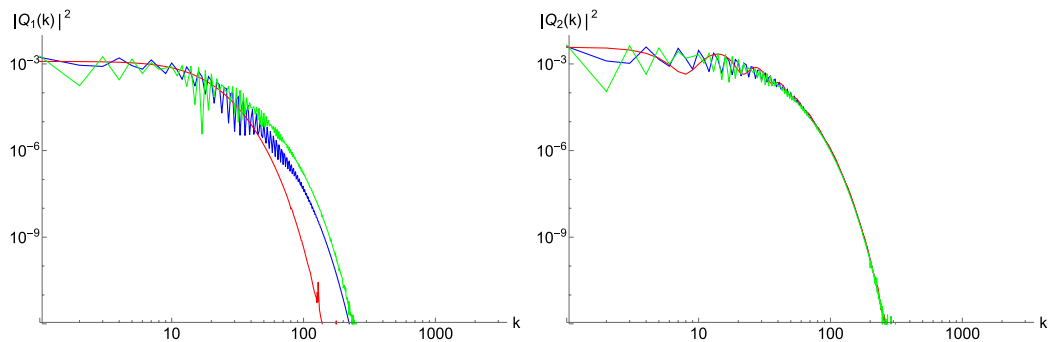


Fig. 3. The intensity spectra for the vector soliton modes Q_1 and Q_2 at 3 different times: $t = 0$ (blue), $t = 60K$ (red) and $t = 120K$ (green). At $t = 60k$ an inelastic vector Manakov collision has already occurred resulting in a single soliton in Q_1 . This results in a narrower, less oscillatory intensity spectrum (red curve). (For interpretation of the references to color in this figure legend, the reader is referred to the web version of this article.)

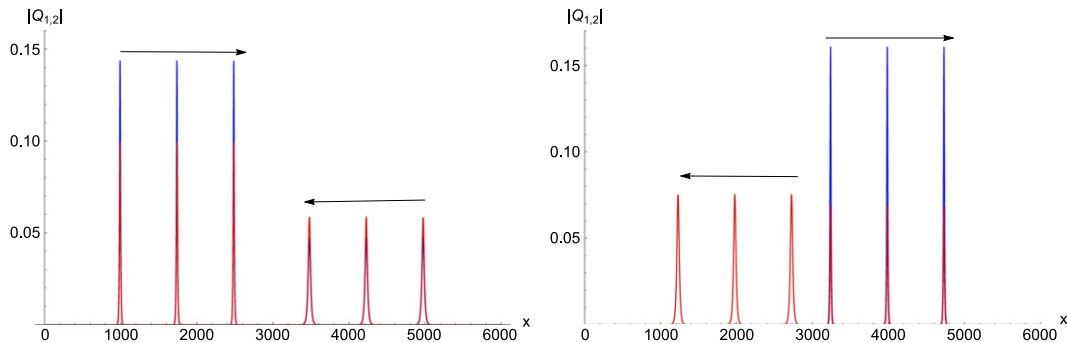


Fig. 4. The collisional evolution of Manakov vector solitons for large amplitudes and speeds. (a) (left figure) The pre-collision states are at times $t = 0, t = 5K, t = 10K$ while the post-collision states (b) (right figure) are at times $t = 15K, t = 20K, t = 25K$. The first polarization amplitude 2-soliton $|Q_1(x, t)|$ is in blue (these are embedded in the Q_2 solitons and so hence not that visible). The orthogonal polarization 2-soliton $|Q_2(x, t)|$ is in red. The inelastic soliton collision occurs for specially chosen soliton amplitudes and speeds, and in this case the position collision soliton for $|Q_1(x, t)| = 0$ for $x < 3000$ is totally absent. Simulations performed on a grid $L = 6000$, under periodic boundary conditions. The amplitudes are now a factor of 4–8 greater than before and the speeds nearly a factor of 2 greater. Higher amplitudes and speeds can be run but will eventually require larger spatial grids to resolve the very sharp solitons. (For interpretation of the references to color in this figure legend, the reader is referred to the web version of this article.)

Eq. (9) can be satisfied, see Fig. 4, where again the post-collision soliton in $|Q_1|$ is annihilated at the first collision. It should be noted that as the soliton amplitudes increase they become more sharply focused spatially. Even though higher amplitudes can be handled by our new Dirac-based QLG algorithm one will eventually need to increase the grid resolution.

The long-time evolution (to $t_{max} = 400K$) of the soliton peaks is shown in Fig. 5. There are more collisions since the soliton speed is increased by almost a factor of 2. The quite precise step-function behavior in the maxima of the amplitudes $|Q_{1,2}|$ in Fig. 5 illustrate the accuracy of the QLG simulation. For example, in between collisions we find (for a different set of collision parameters) that the average peak in $|Q_1| = 0.1607$, with standard deviation $\sigma_1 = 1.85e-04$, while for the

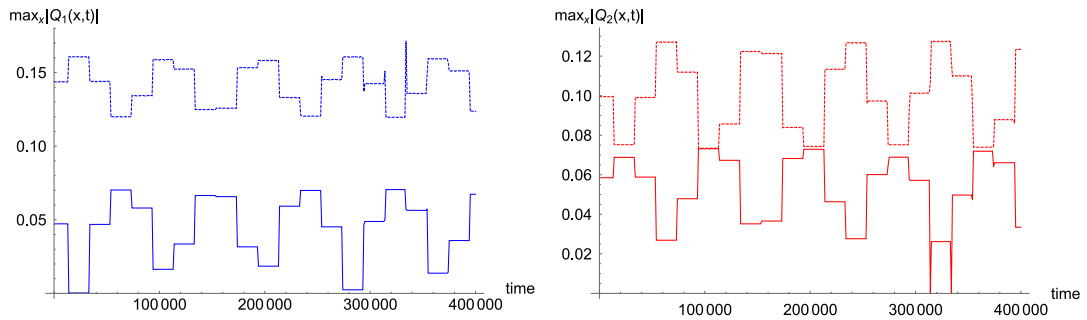


Fig. 5. A plot of the time evolution of the vector 2-soliton peaks, $\max_{1 \leq x \leq L} |Q_n(x, t)|$, $n = 1, 2$, in each mode. Vector soliton–soliton collisions occur whenever the peaks spike. Between collisions the vector two-solitons are invariant. For the parameters chosen, an inelastic Manakov soliton collision occurs only for $t \sim 20K$, with the subsequent loss of one of the solitons. This soliton reappears following the next vector soliton–soliton overlap collision. The dashed curves are for the higher amplitude soliton within that particular mode, while the solid curve is for the lower soliton amplitude.

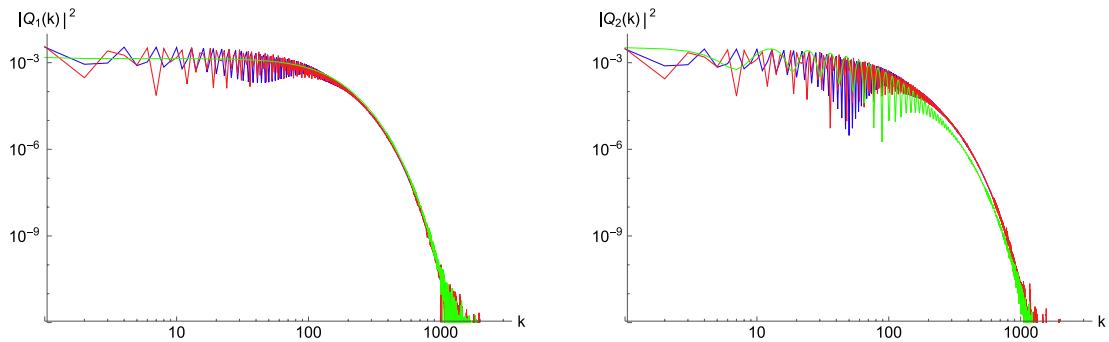


Fig. 6. The intensity spectra for the vector soliton modes Q_1 and Q_2 at 3 different times: $t = 0$ (blue), $t = 5k$ (red) and $t = 15k$ (green). At $t = 15k$ an inelastic vector Manakov collision has already occurred resulting in a single soliton in Q_1 . (For interpretation of the references to color in this figure legend, the reader is referred to the web version of this article.)

average peak in $|Q_2| = 0.0752$, with standard deviation $\sigma_2 = 2.12e-05$. In the next post-collision phase, the average peak in $|Q_1| = 0.1440$, with standard deviation $\sigma_1 = 1.66e-04$, with the average peak in $|Q_2| = 0.099$, and standard deviation $\sigma_2 = 1.14e-04$.

The corresponding intensity spectrum in each mode is shown for the integrable Manakov vector solitons in Fig. 6. For these sharper solitons the spectrum now extends further in wavenumber k space and is flatter for a more extended range of small k than for the broader lower amplitude solitons shown in Fig. 3.

3.3. Nonintegrable vector soliton collisions with radiation, $B = 1.95$ in Eq. (3)

If $B = 1$ in Eq. (3), then the coupled NLS equations are exactly integrable, giving rise to both elastic and (in a special case) inelastic Manakov vector soliton collisions. However, if $B \neq 1$, the coupled NLS equations are non-integrable. Here we present simulations using the same parameters as in the previous section B , but now increasing the birefringence parameter to $B = 1.95$. While there seems to be some mode-locking, quite rapidly one of the initial solitons is destroyed with significant radiation (see Fig. 7).

If one now follows the evolution of the peaks in Q_n in time one quickly sees the non-integrable nature of the coupled NLS equation (3) when $B \neq 1$: there are no flat horizontal sections for any time intervals, Fig. 8.

The radiation lifts the intensity spectrum for large k , as clearly seen in Fig. 9.

4. Conclusion

We have further benchmarked a new quantum lattice gas algorithm on exactly integrable nonlinear 1D soliton systems. In particular, we have modeled the vector Manakov solitons which are exactly soluble using the Hirota method on the coupled set of NLS equations. We have also considered the non-integrable case with the algorithm preserving the vector normalization to 8 significant figures. This new quantum lattice gas utilizes unitary collide-stream operations on qubit amplitudes. The collision operator is deduced from the Dirac equation [28] where the particle’s mass, a Lorentz invariant scalar quantity, is augmented by an additional scalar quantity that for the coupled NLS system is spatially dependent: $m \rightarrow m + \delta m(x)$. When the additional mass term is equated to an effective nonlinear potential, we represent an effective potential as a Lorentz scalar quantity. Indeed this extra mass term $\delta m(x)$ models the $|Q|^4$ term that appears in the corresponding

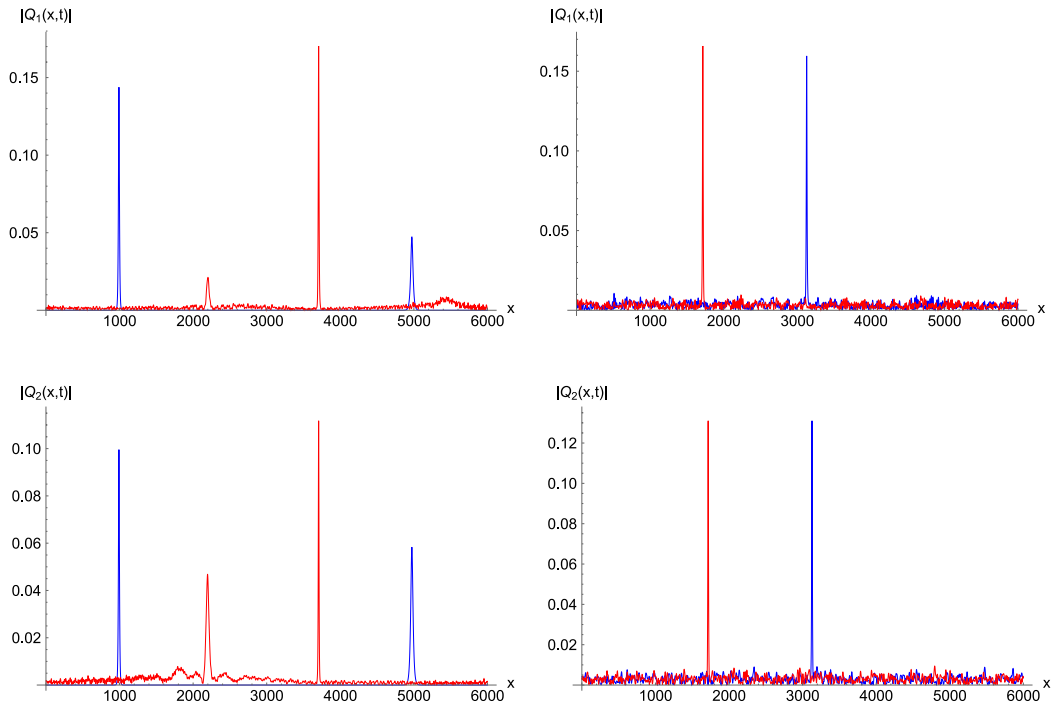


Fig. 7. Upper figures: Time snapshots of $|Q_1(x, t_i)|$: Left Plot: the initial 2 sech-profiles at $t_0 = 0$ (blue), and at $t = 20K$ (red). Right Plot: at times $t = 120K$ (blue) and $t = 230K$ (red). Lower figures: Time snapshots of $|Q_2(x, t_i)|$: Left Plot: the initial 2 sech-profiles at $t_0 = 0$ (blue), and at $t = 20K$ (red). Right Plot: at times $t = 120K$ (blue) and $t = 230K$ (red). One sees mode-locking of quasi-solitons as well as considerable radiation. The normalizations $\int |Q_i(x, t)|^2 dx = const.$ are preserved to at least 8 significant figures for all times. The birefringent coefficient $B = 1.95$ for the coupled non-integrable NLS system. (For interpretation of the references to color in this figure legend, the reader is referred to the web version of this article.)

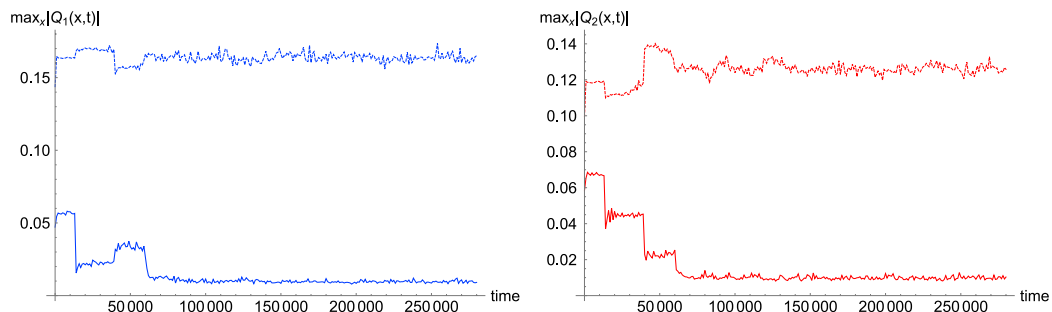


Fig. 8. A plot of the time evolution of the vector 2-soliton peaks, $\max_{1 \leq x \leq L} |Q_n(x, t)|$, $n = 1, 2$, in each mode. One notes mode-locking of the main sharp quasi-soliton and the excitation of radiation modes.

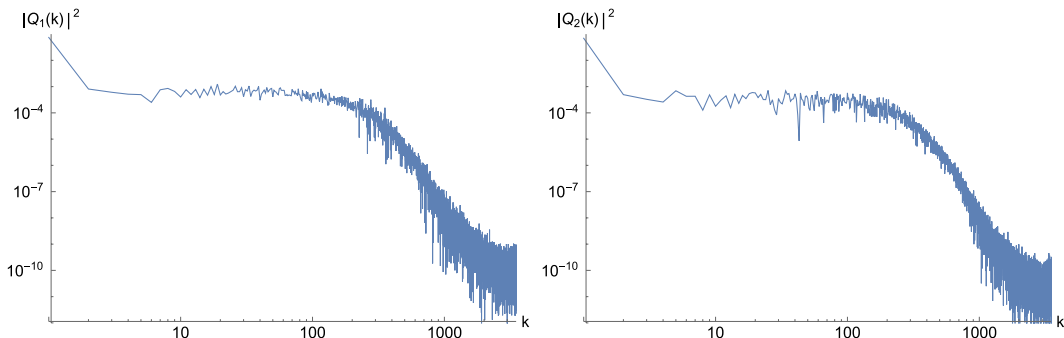


Fig. 9. The intensity spectra for the vector soliton modes Q_1 and Q_2 at $t = 230K$. For small k , $k < 100$, the spectrum is flat while for large k , $k > 400$, the spectrum exhibits a power law structure: $k^{-20/3}$.

Lagrangian. Such a term is well known to preserve the Lorentz invariance. The nonrelativistic limit is then achieved by employing a kinetic energy/potential energy decomposition interleaving scheme that uses a quantum algorithmic protocol of multiple unitary stream and collide operations at each time step. In this way, we can achieve high numerical accuracy even when the coupling constant is large. The new Dirac-based QLG algorithm is tested against the exactly soluble vector Manakov soliton problem, with excellent agreement with theory. More importantly, the soliton amplitudes under this Dirac-based algorithm are an order of magnitude greater than that permitted by our earlier $\sqrt{\text{SWAP}}$ -collision QLG algorithm. This should permit meaningful simulations of spinor BECs.

Acknowledgments

This work was supported, in part, by the Air Force Office of Scientific Research and National Science Foundation. While the Dirac QLG computations reported here, which solve the 1D Manakov set of coupled NLS equations, were performed on a laptop computer, its 3D QLG algorithms (with the $\sqrt{\text{SWAP}}$ collision operator) have been run on supercomputing facilities at DoD, DoE and NSF. Indeed, we have had timings that scale perfectly on the full 786432 cores of the IBM/BlueGene Q Mira.

References

- [1] Richard P. Feynman, There's plenty of room at the bottom. Caltech Engineering and Science, February 1960. This is a transcript of Feynman's talk given on December 29, 1959 at the Annual Meeting of the American Physical Society.
- [2] Richard P. Feynman, Simulating physics with computers, *Internat. J. Theoret. Phys.* 21 (6–7) (1982) 467–488.
- [3] G.V. Riazanov, The Feynman path integral for the Dirac equation, *Sov. Phys. JETP* 6 (33) (1958) 7.
- [4] Richard P. Feynman, Geometry of Dirac equ. in 1 dimension. California Institute of Technology CIT archives, (13.3), February 1946.
- [5] Richard P. Feynman, A.R. Hibbs, *Quantum Mechanics and Path Integrals*, McGraw-Hill, 1965, Problem 2–6 on page 34.
- [6] Gerard 't Hooft, Equivalence relations between deterministic and quantum mechanical systems, *J. Stat. Phys.* 53 (1–2) (1988) 323–344.
- [7] Gerard 't Hooft, Quantum mechanical behaviour in a deterministic model, *Found. Phys. Lett.* 10 (2) (1997) 105–111.
- [8] Jeffrey Yepez, Short introduction to quantum computation, in: USAF Technical Report ADA434366, Proceedings of the 1996 AFOSR Meeting of Computational and Applied Mathematics, Air Force Phillips Laboratory, 1996.
- [9] Jeffrey Yepez, New world vistas: New models of computation, lattice based quantum computation. USAF Technical Report (DTIC ADA421712), 1996.
- [10] Iwo Bialynicki-Birula, Weyl, Dirac, and Maxwell equations on a lattice as unitary cellular automata, *Phys. Rev. D* 49 (12) (1994) 6920–6927.
- [11] Paul Benioff, Quantum ballistic evolution in quantum mechanics: Application to quantum computers, *Phys. Rev. A* 54 (2) (1996) 1106–1123.
- [12] David A. Meyer, Quantum mechanics of lattice gas automata: One-particle plane waves and potentials, *Phys. Rev. E* 55 (5) (1997) 5261–5269.
- [13] Bruce M. Boghosian, Washington Taylor, Quantum lattice–gas model for the many-particle Schrödinger equation in d dimensions, *Phys. Rev. E* 57 (1) (1998) 54–66.
- [14] Jeffrey Yepez, Lattice gas dynamics: volume III quantum algorithms for computational physics. Technical Report AFRL-VS-HA-TR-2006-1143, Air Force Research Laboratory, AFRL/RV Hanscom AFB, MA 01731, 2007, DTIC ADA474659.
- [15] A. Oganegov, G. Vahala, L. Vahala, J. Yepez, M. Soe, B. Zhang, Unitary quantum lattice gas algorithm generated from the Dirac collision operator for 1D soliton–soliton collisions, *Rad. Eff. Defects Solids* 170 (2015) 55–64.
- [16] R. Radhakrishnan, K. Lakshmanan, J. Hietarinta, Inelastic collision and switching of coupled bright solitons in optical fibers, *Phys. Rev. E* 56 (1997) 2213.
- [17] M.K. Jakubowski, K. Steiglitz, R. Squier, State transformations of colliding optical solitons and possible applications to computation in bulk media, *Phys. Rev. E* 58 (1998) 6752.
- [18] K. Steiglitz, Time-gated Manakov spatial solitons are computationally universal, *Phys. Rev. E* 63 (2001) 016608.
- [19] K. Steiglitz, Multi-scale collision cycles of Manakov spatial solitons, *Phys. Rev. E* 63 (2001) 046607.
- [20] G. Vahala, L. Vahala, J. Yepez, Inelastic vector soliton collisions: a lattice-based quantum representation, *Proc. R. Soc.* 362 (2004) 1677.
- [21] S. Succi, R. Benzi, Lattice Boltzmann equation for quantum mechanics, *Physica D* 69 (1993) 327.
- [22] S. Palpacelli, S. Succi, The quantum lattice Boltzmann equation: recent developments, *Commun. Comput. Phys.* 4 (2008) 980.
- [23] F. Fillion-Gourdeau, H.J. Herrmann, M. Mendoza, S. Palpacelli, S. Succi, Formal analogy between the Dirac equation in its Majorana form and the discrete-velocity version of the Boltzmann kinetic equation, *Phys. Rev. Lett.* 113 (2013) 160602.
- [24] Adriano Barenco, Charles H. Bennett, Richard Cleve, David P. DeVincenzo, Norman H. Margolus, Peter W. Shor, Tycho Sleator, John Smolin, Harald Weinfurter, Elementary gates for quantum computation, *Phys. Rev. A* 52 (5) (1995) 3457–3467.
- [25] P.J. Dellar, D. Lapitski, S. Palpacelli, S. Succi, Isotropy of three-dimensional quantum lattice Boltzmann schemes, *Phys. Rev. E* 83 (2011) 046706.
- [26] Sauro Succi, *The Lattice Boltzmann Equation for Fluid Dynamics and Beyond*, Clarendon Press, New York, 2001.
- [27] Jeffrey Yepez, *Quantum Inf. Process.* 4 (6) (2005) 471.
- [28] Jeffrey Yepez, Quantum lattice gas model of Dirac particles in $1 + 1$ dimensions, 2013. arxiv:1307.3595v1, quant-ph.